

Chapter 2

Phase Diagram and Excitations of the Jaynes-Cummings-Hubbard Model

Sebastian Schmidt and Gianni Blatter

Abstract The Jaynes-Cummings-Hubbard model (JCHM) has emerged as a fundamental model at the interface of quantum optics and condensed matter physics. It describes strongly correlated photons in a coupled qubit-cavity array and predicts a superfluid-Mott insulator transition of polaritons under quasi-equilibrium conditions. Here, we review recent analytical as well as numerical results for the phase diagram, elementary excitations and critical exponents of the JCHM and compare them to closely related models such as the Bose-Hubbard and the Dicke model. We comment on the fate of these results in open dissipative systems and outline schemes for their experimental verifiability.

2.1 Introduction

Since its proposal by Greentree [1] and Angelakis [2], the study of the Jaynes-Cummings-Hubbard model (JCHM) has become an active and versatile research field bridging two areas of modern physics: quantum optics and condensed matter. The JCHM describes photons hopping in an array of coupled cavities and locally interacting with qubits. Its Hamiltonian is given by

$$H = \sum_i h_i^{\text{JC}} - J \sum_{\langle ij \rangle} a_i^\dagger a_j, \quad (2.1)$$

where h_i^{JC} denotes the local Jaynes-Cummings Hamiltonian

$$h_i^{\text{JC}} = \omega_c a_i^\dagger a_i + \omega_x \sigma_i^+ \sigma_i^- + g(\sigma_i^+ a_i + \sigma_i^- a_i^\dagger) \quad (2.2)$$

S. Schmidt (✉) · G. Blatter
Institute for Theoretical Physics, Eth Zurich, Zürich, Switzerland
e-mail: schmidts@phys.ethz.ch

G. Blatter
e-mail: blatterj@phys.ethz.ch

with site index i , photon creation (annihilation) operators $a_i^{(\dagger)}$ and qubit raising (lowering) operators $\sigma_i^{+(-)}$. The cavity mode frequency is ω_c , the two qubit levels are separated by the energy ω_x and g denotes the light-matter coupling strength (we set $\hbar = 1$). The second term in (2.1) describes photon hopping between nearest neighbour sites with amplitude J . The light-matter interaction mediated by g leads to the formation of polariton quasiparticles and introduces a nonlinearity into the spectrum of the JCHM. Depending on the perspective, the JCHM can thus be viewed as a lattice model for dressed photons, which gain an effective mass through cavity confinement and are interacting due to the nonlinearity mediated by the qubits or as an effective spin lattice model, where effective spin-spin interactions are mediated by photon exchange between distant cavities [2–5].

The physics of coupled cavity arrays is very rich reaching from strong correlation phenomena and driven dissipative phase transitions, e.g., superfluid-Mott insulator type transitions [1, 2, 6–28], self-trapping and Josephson-like phenomena [29–33], crystalline-like phases of light [34–37] or fermionization of photons [38–40] to topological phenomena associated with the engineering of artificial gauge fields [41–48], edge or Majorana-like modes [48–52] or the Fractional quantum Hall effect [53–56]. For recent reviews on the topic see Refs. [57–61].

One of the major appeals of the JCHM is the possibility to engineer this model bottom-up in solid-state cavity or circuit QED architectures. Photonic lattices (without the coupling to qubits) have already been engineered on a large scale with only little disorder in cavity frequencies (as compared to the hopping rate) [43, 62]. Effective photon-photon interactions in a coupled qubit-cavity array were realised very recently as well: In Ref. [33] a non-equilibrium delocalization-localization transition (self-trapping) of photons has been observed as originally predicted in Ref. [31]. The experiment was based on a two site version of the JCHM, i.e., a so-called Jaynes Cummings dimer. It demonstrates a new scalable architecture for quantum simulation of non-equilibrium many-body systems with a high-level of control over coherent and dissipative dynamics.

A chemical potential for polaritons?

The global $U(1)$ symmetry of the JCHM preserves the total number of polaritons $N = \sum_i (a_i^\dagger a_i + \sigma_i^+ \sigma_i^-)$. It is thus convenient to introduce a chemical potential μ , which fixes the number of polaritons [1, 2], i.e.,

$$H \rightarrow H - \mu N, \quad (2.3)$$

Introducing such a chemical potential assumes the existence of a grand-canonical ensemble and thus thermalisation. However, photonic systems are driven dissipative systems and typically settle in a non-equilibrium steady state, which can be far from equilibrium. It is thus important to identify situations under which calculations in the grand-canonical ensemble are meaningful and experimentally verifiable. Below we briefly discuss two possible experimental schemes.

The first situation considers incoherent pumping of a polaritonic system with weak dissipation. For example, photons confined in a dye-filled optical micro-cavity

condense into an equilibrium Bose-Einstein condensate with grand-canonical number statistics [63–65]. In such a system, effective thermalisation of photons occurs through emission and absorption by dye-molecules, which themselves are coupled to a large thermal phonon reservoir. Possible extensions of photonic condensates to periodic photonic lattices are discussed in Ref. [66]. Note, that such incoherent pumping mechanisms can also be realised in strongly interacting light-matter systems based on exciton-polaritons [67] and superconducting qubits [68].

The second situation considers quenched dynamics. For example, a coupled qubit-cavity array can be initialized in a Mott-like state using a large coherent pulse [19]. Observing the subsequent decay of such a special initial state under weak dissipation reveals the quantum phase diagram of the Hamiltonian under equilibrium conditions, i.e. the coherence of the system at long times approaches zero for $J < J_c$, i.e., in the Mott phase, while it is nonzero for $J > J_c$, i.e., in the superfluid phase (J_c denotes the critical hopping strength of the quantum phase transition in equilibrium). Note, that the distinction between Mott and superfluid phases becomes sharp only when dissipation vanishes, but otherwise is smoothened and washed out (similar to finite temperature effects for ultra cold atoms in optical lattices as described by the Bose-Hubbard model (BMH) [69]).

In this review we focus on the superfluid-Mott insulator transition of polaritons under (quasi-) equilibrium conditions. In Chap. 2, we discuss the atomic limit ($J = 0$) and simple perturbative estimates for the phase diagram of the JCHM. In Chap. 3, we show that a linked-cluster expansion of the photonic Matsubara Green's function can be utilised to calculate the quantum phase diagram and elementary excitations of the JCHM in the Mott phase. In Sect. 2.3 we generalise such a strong coupling approach to the superfluid phase using a slave-boson technique. In Chap. 4 we briefly summarise the results of exact Quantum-Monte-Carlo simulations determining the universality class and critical exponents of the JCHM. Finally, in Chap. 5 we discuss an intricate relation between the SF-MI transition in the JCHM and the super-radiance phase transition in a multi-mode Dicke model. In particular, we show that a weak-coupling mean-field theory predicts the existence of a single Mott lobe even in the absence of an underlying cavity array.

2.2 Degenerate Perturbation Theory

In the atomic limit ($J = 0$) the eigenstates of the Hamiltonian (2.1) are the dressed polariton states $|n\sigma\rangle$ labelled by the polariton number n and upper/lower branch index $\sigma = \pm$. For $n > 0$ they can be written as a superposition of a Fock state with n photons plus atomic ground state $|n, g\rangle$ and $(n - 1)$ photons with the atom in its excited state $|(n - 1), e\rangle$,

$$\begin{aligned} |n+\rangle &= \sin \theta_n |n, g\rangle + \cos \theta_n |(n - 1), e\rangle, \\ |n-\rangle &= \cos \theta_n |n, g\rangle - \sin \theta_n |(n - 1), e\rangle, \end{aligned} \quad (2.4)$$

with the angle $\tan \theta_n = 2g\sqrt{n}/(\delta + 2\chi_n)$, $\chi_n = \sqrt{g^2n + \delta^2/4}$ and the detuning parameter $\delta = \omega_c - \omega_x$. The corresponding eigenvalues are

$$\epsilon_n^\sigma = -(\mu - \omega_c)n - \delta/2 + \sigma \chi_n, \quad \sigma = \pm. \quad (2.5)$$

The zero polariton state $|0-\rangle = |0, g\rangle$ is a special case with $\epsilon_0^- = 0$. Note, that upper and lower polariton energies are separated by the so-called Rabi splitting $\Omega_n = 2\sqrt{g^2n + \delta^2/4}$.

Starting from the atomic limit result in Eqs. (2.4) and (2.5) we can obtain a rough estimate for the quantum phase diagram of the JCHM at small tunnelling $J \ll g$ by calculating the excitation energies in straightforward degenerate perturbation theory. To first order, the chemical potentials at which the addition/removal of a lower polariton costs no energy is given by (we assume a hypercubic lattice in D dimensions)

$$\begin{aligned} \mu_p - \omega_c &= \chi_n - \chi_{n+1} - 2DJ(f_{n+1}^{--})^2 + \mathcal{O}(J^2/g), \\ \mu_h - \omega_c &= \chi_{n-1} - \chi_n + 2DJ(f_n^{--})^2 + \mathcal{O}(J^2/g). \end{aligned} \quad (2.6)$$

The two equations in (2.6) define the upper and lower phase boundary in the quantum phase diagram in Fig. 2.1 for small values of the hopping parameter J/g . The point where the two lines meet (i.e., $\mu_p = \mu_h$) is $J_c \sim 0.1g$ for $n = 1$ and represents an upper limit for the size of the first Mott lobe. By going to higher order in the perturbative expansion for the ground-state energy and subsequent resummation of

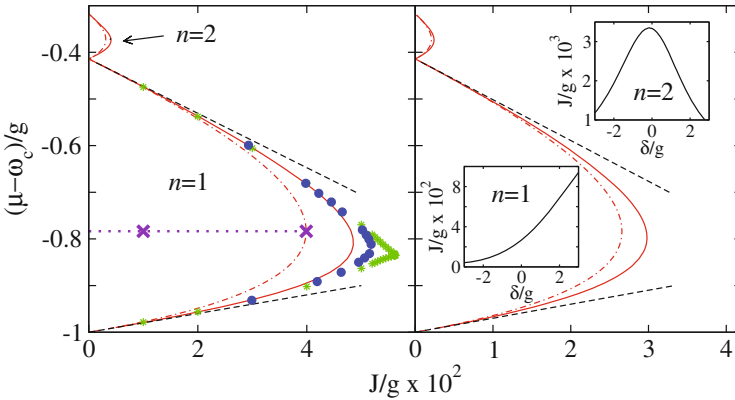


Fig. 2.1 Quantum phase diagram for a hypercubic lattice in $D = 2$ (left figure) and $D = 3$ (right figure). We show two Mott lobes for $n = 1, 2$ at zero detuning $\delta = 0$. We compare first-order perturbation theory (dashed), RPA (dot-dashed) and quantum fluctuations (solid) with recent results from a quantum Monte-Carlo (filled dots) [11] and variational cluster (stars) [9] approach. The two crosses (left figure) connected by the dotted line mark the parameter values used in Fig. 2.2. The insets show the critical hopping strength J_c/g at the tip of the lobe as a function of the detuning δ for $n = 1$ and $n = 2$ calculated within strong-coupling RPA in $D = 3$ dimensions. Figure taken with permission from Ref. [12]

the diverging strong-coupling series, e.g., via variational perturbation theory (VPT) [70, 71], one could in principle determine the exact location of the phase boundary. This has recently been achieved for the BHM [72, 73].

2.3 Greens Function Approach

In this section, we study the photonic Matsubara Green's function

$$G_{ij}(\tau; \tau') = -\langle \mathcal{T} a_i(\tau) \bar{a}_j(\tau') \rangle \quad (2.7)$$

with the time-ordering operator \mathcal{T} and the Heisenberg operator $\bar{a}_j(\tau') = e^{H\tau'} a_j^\dagger e^{-H\tau'}$. A suitable method for the evaluation of the Matsubara Green's function is a linked-cluster expansion in terms of local cumulants originally developed by Metzner et al. [74] for the Fermi-Hubbard model (FHM) and more recently applied to the BHM [75].

First, we study the atomic limit ($J = 0$). For $J = 0$ the Matsubara Green's function is local and given by

$$G_{0ij}(\tau; \tau') = G_{0i}(\tau; \tau') \delta_{ij} = -\langle \mathcal{T} a_i(\tau) \bar{a}_i(\tau') \rangle_0 \delta_{ij}, \quad (2.8)$$

where the average $\langle \dots \rangle_0$ is taken with respect to the eigenstates of the local Hamiltonian in Eq. (2.4). We consider a spatially homogeneous system, drop the site index i and obtain after a Fourier transformation

$$G_0(\omega_m) = \sum_{n,\sigma,\mu} \frac{e^{-\beta\epsilon_n^\sigma}}{Z} \left(\frac{z_{n+1}^{\mu\sigma}}{\Delta_{n+1}^{\mu\sigma} - i\omega_m} - \frac{z_n^{\sigma\mu}}{\Delta_n^{\sigma\mu} - i\omega_m} \right) \quad (2.9)$$

with the partition function $Z = \sum_{n\sigma} e^{-\beta\epsilon_n^\sigma}$ and bosonic Matsubara frequencies $\omega_m = 2\pi m/\beta$ (here, $\beta = 1/(k_B T)$ with temperature T and Boltzmann constant k_B). The spectral weights in (2.9) are defined as $z_n^{\mu\sigma} = (f_n^{\mu\sigma})^2$ with the matrix elements $f_n^{\sigma\nu} = \langle n\sigma | a^\dagger | (n-1)\nu \rangle$. At zero detuning ($\delta = 0$) they are given by $f_n^{\sigma\nu} = (\sqrt{n} + \sigma\nu\sqrt{n-1})/2$ for $n > 1$ ($f_1^{\sigma-} = 1/\sqrt{2}$).

Following the recipe in Metzner et al. [74], each term of the linked-cluster expansion can be written diagrammatically in terms of n -particle cumulants represented by $2n$ -leg vertices and tunneling matrix elements symbolized by propagating lines connecting two vertices. The strong-coupling expansion provided by the linked-cluster method is applicable to the JCHM because (i) the atomic limit Hamiltonian is local, and (ii) anomalous averages of the photon operator with respect to the eigenstates of the local Hamiltonian vanish, i.e., $\langle n\sigma | (a^\dagger)^k | n\sigma \rangle = 0$ for $k \in \mathbb{N}$ (since a single photon excitation always changes the polariton number). In this case an infinite set of diagrams can be summed by calculating the irreducible part of the Green's function $K(\mathbf{k}, \omega_m)$ which is connected to the full Green's function via the equation

$$G(\mathbf{k}, \omega_m) = K(\mathbf{k}, \omega_m) / [1 - J(\mathbf{k})K(\mathbf{k}, \omega_m)] \quad (2.10)$$

with the lattice dispersion $J(\mathbf{k})$, e.g., for a hypercubic lattice $J(\mathbf{k}) = 2J \sum_{i=1}^D \cos \mathbf{k} \cdot \mathbf{a}_i$ (\mathbf{a}_i denotes a lattice vector). To second order in J we obtain

$$\begin{aligned} K(\omega_m) &= \text{---} \bullet \text{---} + \text{---} \bullet \text{---} \text{---} \bullet \text{---} \\ &= G_0(\omega_m) + 2DJ^2 Q(\omega_m) \end{aligned} \quad (2.11)$$

with

$$Q(\omega_m) = \int_0^\beta d\tau d\tau_1 d\tau_2 C^{(2)}(\tau_1 0; \tau_2 \tau) G_0(\tau_2; \tau_1) e^{i\omega_m \tau}. \quad (2.12)$$

The quantum fluctuation correction $Q(\omega_m)$ involves the two-particle cumulant $C^{(2)}(\tau_1 0; \tau_2 \tau)$, which is related to the local (atomic limit) two-particle Green's function $G_0^{(2)}(\tau_1 0; \tau_2 \tau) = \langle T a_i(\tau_1) a_i(0) \bar{a}_i(\tau_2) \bar{a}_i(\tau) \rangle_0$ via

$$C^{(2)}(\tau_1 0; \tau_2 \tau) = G_0^{(2)}(\tau_1 0; \tau_2 \tau) - G_0(\tau_1; \tau_2) G_0(0; \tau) - G_0(\tau_1; \tau) G_0(0; \tau_2). \quad (2.13)$$

The algebraic expressions for the two-particle cumulant and the quantum correction $Q(\omega_m)$ are lengthy, but can be calculated in a straightforward manner [12].

The object of interest is the inverse Greens function which tells us immediately about the phase boundary $G^{-1}(\mathbf{0}, 0)|_{J_c(\mu)} = 0$ and the dispersion relation $G^{-1}(\mathbf{k}, i\omega_m \rightarrow \omega + i0^+) = 0$. It is thus convenient to introduce the strong-coupling self-energy $\Sigma(\mathbf{k}, \omega_m)$ via $G(\mathbf{k}, \omega_m)^{-1} = G_0(\omega_m)^{-1} - \Sigma(\mathbf{k}, \omega_m)$. From (2.11) we obtain to second order

$$\Sigma(\mathbf{k}, \omega_m) = J(\mathbf{k}) + 2DJ^2 Q(\omega_m) / G_0(\omega_m). \quad (2.14)$$

The first term on the r.h.s. is usually called the strong-coupling random-phase approximation (RPA), whereas the second term denotes the leading correction due to quantum fluctuations. The RPA corresponds to a summation of all self-avoiding walks (chain diagrams) through the lattice. The leading quantum correction includes in addition all one-time forward/backward hopping processes (bubble diagrams) between two neighbored sites.

Although we have carried out our calculations at finite temperature, we will only consider the $T = 0$ case from now on. At the quantum phase transition the energy of long wavelength fluctuations vanishes and we obtain an explicit expression for the critical hopping strength

$$J_c^{-1} = D G_0(0) \left(1 + \sqrt{1 + 2Q(0)/(D G_0^3(0))} \right). \quad (2.15)$$

If we ignore the second term under the square root in (2.15) we obtain the RPA phase boundary $1/J_c = 2D G_0(0)$ shown as a dashed-dotted line in Fig. 2.1. This result agrees exactly with the phase boundary as obtained from a numerical decoupling mean-field approach [1, 2]. The inclusion of quantum fluctuations in (2.15) leads to an improved phase boundary (solid line in Fig. 2.1). In two dimensions the result in Eq. (2.15) agrees well with Monte-Carlo calculations [11, 20, 22]. There is a small deviation near the tip of the lobe, where quantum corrections are most important. In the right panel of Fig. 2.1 we present quantitatively accurate results for the phase diagram in $D = 3$ (note, that the strong-coupling expansion becomes more accurate in higher dimensions).

We now discuss the elementary excitations of the JCHM in the Mott phase based on the RPA, i.e., by neglecting the second term in (2.14). An analytic continuation of the Matsubara Green's function via $i\omega_n \rightarrow \omega + i0^+$ yields the retarded real-time Green's function. Its poles and residues provide us with the dispersion relations and mode strengths of the fundamental excitations. In general, we obtain four poles, the conventional (Bose-Hubbard like) lower polariton particle (hole) modes $\omega_{(p,h)}^-$ and two modes $\omega_{(p,h)}^+$ which correspond to an upper polariton particle (hole) excitation (conversion modes). The presence of the latter signals a clear deviation from the usual Bose-Hubbard like physics and is due to the composite quasi-particle nature of polaritons.

The conversion modes exist already in the atomic limit, but have been overlooked in early numerical approaches. One reason might be that their bandwidth and strengths are very small as compared to the conventional modes. However, extended numerical studies have confirmed the prediction in [14]. The weakness of the conversion modes throughout the Mott lobe allows us to set their dispersion relations $\omega_{(p,h)}^+$ and mode strength $s_{(p,h)}^+$ approximately equal to $\omega_{(p,h)}^+ \approx \Delta_{(p,h)}^+$ and $s_{(p,h)}^+ \approx z_{(p,h)}^+$ with the atomic-limit particle (hole) gaps $\Delta_p^\sigma \equiv \Delta_{n+1}^{\sigma-}$ ($\Delta_h^\sigma \equiv \Delta_n^{\sigma-}$) and mode strengths $z_p^\sigma \equiv z_{n+1}^{\sigma-}$ ($z_h^\sigma \equiv -z_n^{\sigma-}$), respectively. If we neglect their contribution to the one-particle cumulant (2.9), we can derive simple analytic formulas for the dispersion relations of the conventional modes, i.e.,

$$\omega_{(p,h)}^- = (\Delta_+ - J(\mathbf{k}) z_+ \pm \Omega) / 2 \quad (2.16)$$

with $\Omega = \sqrt{\Delta_-^2 + J(\mathbf{k})^2 z_+^2 - 2J(\mathbf{k}) z_- \Delta_-}$ and the abbreviations $\Delta_\pm = \Delta_p^\pm \pm \Delta_h^\pm$ and $z_\pm = z_p^\pm \pm z_h^\pm$. The strength of the modes are given by

$$s_{(p,h)}^- = \frac{z_+ \omega_{(p,h)}^- - z_{(p,h)}^- \Delta_{(h,p)}^- - z_{(h,p)}^- \Delta_{(p,h)}^-}{\omega_{(p,h)}^- - \omega_{(h,p)}^-}. \quad (2.17)$$

The dispersions in (2.16) are plotted in Fig. 2.2 deep inside the Mott regime and at the tip of the lobe with $n = 1$. As shown in the inset of Fig. 2.2 the energy needed for a conventional excitation is an order of magnitude smaller than for a conversion excitation. The strengths of the conventional modes $s_{(p,h)}^-$ grow with increasing tunneling

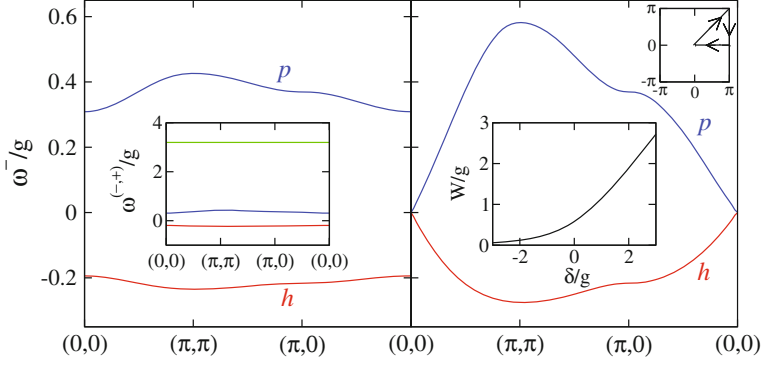


Fig. 2.2 Particle/hole dispersion of the conventional modes $\omega_{(p,h)}^-$ for $D = 2$ and $n = 1$ at zero detuning $\delta = 0$. *Left figure* Deep inside the Mott insulator (see cross in Fig. 2.1) for $(\mu - \omega_c)/g = -0.78$ and $J/g = 0.01$. The inset shows the conventional modes $\omega_{(p,h)}^-$ together with the conversion mode ω_p^+ . *Right figure* At the phase boundary (see cross in Fig. 2.1) for $(\mu - \omega_c)/g = -0.78$ and $J/g = 0.04$. The inset shows the bandwidth W of the conventional particle mode ω_p^- as a function of detuning δ at the tip of the lobe. Figure taken with permission from Ref. [12]

strength while the strengths of the conversion modes $s_{(p,h)}^+$ stay approximately constant. If we are only interested in low energy excitations we can thus indeed neglect the contributions from upper polaritons throughout the Mott phase. They will always remain gapped even at the phase boundary. We will make use of this result in the next section, where we will also calculate the excitation spectra in the superfluid phase using a slave-boson approach.

2.4 Slave-Boson Approach

In the previous section we derived an analytic strong-coupling theory for the phase diagram and the elementary excitations in the Mott phase of the JCHM based on a linked-cluster expansion (LCA) of the Matsubara Greens function. Here, we generalise such a strong-coupling approach to the superfluid phase using a slave-boson technique [18], which was previously applied to the BHM [76].

2.4.1 Slave-Boson Formulation

A convenient starting point is the polariton representation [13] of the boson operator

$$a_i = \sum_{n\sigma\nu} f_n^{\sigma\nu} P_{in-1}^{\nu\dagger} P_{in}^{\sigma} \quad (2.18)$$

in terms of standard algebra operators $P_{in}^{\sigma\dagger} = |n\sigma\rangle_{ii}\langle 0|$ and matrix elements $f_n^{\sigma\nu}$ defined below Eq. (2.9). In this new basis the JCHM becomes

$$H = \sum_i \sum_{n=0}^{\infty} \sum_{\sigma} \epsilon_n^{\sigma} P_{in}^{\sigma\dagger} P_{in}^{\sigma} - J \sum_{\langle ij \rangle} \sum_{n,n'=1} \sum_{\substack{\sigma,\sigma' \\ \nu,\nu'}} f_n^{\sigma\sigma'} f_{n'}^{\nu\nu'} P_{in}^{\sigma\dagger} P_{in-1}^{\sigma'} P_{jn'-1}^{\nu'\dagger} P_{jn'}^{\nu}. \quad (2.19)$$

The upper polariton branch with $\sigma, \sigma' = +$ leads to additional high energy conversion modes in the Mott phase with small spectral weight and bandwidth as discussed in the previous section. We thus neglect the upper branch as well as particle conversion hopping from now on and drop the branch index σ . This leads to the simplified Hamiltonian

$$H = \sum_i \sum_{n=0}^{\infty} \epsilon_n P_{in}^{\dagger} P_{in} - J \sum_{\langle ij \rangle} \sum_{n,n'=1} f_n f_{n'} P_{in}^{\dagger} P_{in-1} P_{jn'-1}^{\dagger} P_{jn'}. \quad (2.20)$$

with $\epsilon_n \equiv \epsilon_n^-$ and $f_n \equiv f_n^{--}$.

2.4.2 Gutzwiller Ansatz

In order to calculate the phase boundary and static observables in the superfluid phase near a Mott lobe with filling $n \geq 1$, we restrict the Hilbert space to states with n and $n \pm 1$ bosons and make a Gutzwiller Ansatz for the ground-state wave function

$$|\psi\rangle = \prod_i [\cos(\theta) P_{i0}^{\dagger} + \sin(\theta) (\sin(\chi) P_{i-1}^{\dagger} + \cos(\chi) P_{i1}^{\dagger})] |0\rangle,$$

where we also dropped the index n and changed the notation to $P_{i\alpha}^{\dagger} \equiv P_{in+\alpha}^{\dagger}$, $\epsilon_{n+\alpha} \equiv \epsilon_{\alpha}$, and $f_{n+\alpha} \equiv f_{\alpha}$. Note, that this variational wave function is normalized to unity and satisfies the completeness relation, i.e.

$$\sum_{n\sigma} P_{in}^{\sigma\dagger} P_{in}^{\sigma} = 1. \quad (2.21)$$

It is straightforward to show that if the constraint (2.21) is fulfilled, the polariton operators also obey bosonic commutation relations.

The expectation value $\epsilon_{\text{var}} = \langle \psi | H | \psi \rangle$ yields the variational energy

$$\begin{aligned} \epsilon_{\text{var}} = & \epsilon_0 \cos(\theta)^2 + \sin(\theta)^2 [\epsilon_{-1} \sin(\chi)^2 + \epsilon_1 \cos(\chi)^2] \\ & - JD/2 \sin(2\theta)^2 [f_0 \cos(\chi) + f_{-1} \sin(\chi)]^2, \end{aligned} \quad (2.22)$$

which has to be minimized with respect to the variational parameters θ and χ (here, D denotes the dimension of a hypercubic lattice), yielding

$$\tan(2\chi) = \frac{4JDf_0f_1 \cos(\theta)^2}{\epsilon_{-1} - \epsilon_1 + 2JD(f_1^2 - f_0^2) \cos(\theta)^2} \quad (2.23)$$

and

$$\cos(2\theta) = \frac{1}{2JD} \frac{\epsilon_1 \cos(\chi)^2 + \epsilon_{-1} \sin(\chi)^2 - \epsilon_0}{[f_0 \sin(\chi) + f_1 \cos(\chi)]^2}. \quad (2.24)$$

The lobe boundaries are then determined by the vanishing of the order parameter

$$\phi_c = \langle \psi | a | \psi \rangle = \sin(\theta) [f_0 \sin(\chi) + f_1 \cos(\chi)]^2 / 2. \quad (2.25)$$

Setting $\phi_c = 0$ (i.e., $\theta = 0$) in (2.23) and (2.24) and eliminating χ yields the relation

$$\epsilon_{-1} - \epsilon_1 = -Jz(f_1^2 - f_0^2) \pm \sqrt{Q} \quad (2.26)$$

with

$$Q = U^2 - 2Jz(f_0^2 + f_1^2)U + J^2z^2(f_1^2 - f_0^2)^2 \quad (2.27)$$

and

$$U = \epsilon_{-1} - 2\epsilon_0 + \epsilon_1. \quad (2.28)$$

Equation (2.26) constitutes an expression for the mean-field boundaries of the Mott lobes in the JCHM shown in Fig. 2.3 (the energies ϵ_α contain the chemical potential). Note, that they agree exactly with those obtained from the RPA in the previous section.

2.4.3 Quadratic Fluctuations

In order to find the elementary excitations we define a new set of operators $\mathbf{R}^\dagger = (G_i^\dagger, E_{1i}^\dagger, E_{2i}^\dagger)^T$, which is obtained from the original polariton basis $\mathbf{P}^\dagger = (P_{i0}^\dagger, P_{i-1}^\dagger, P_{i1}^\dagger)^T$ via a unitary transformation $\mathbf{R}^\dagger = T\mathbf{P}^\dagger$ with

$$T = \begin{pmatrix} \cos(\theta) & \sin(\theta) \cos(\chi) & \sin(\theta) \sin(\chi) \\ -\sin(\theta) & \cos(\theta) \cos(\chi) & \cos(\theta) \sin(\chi) \\ 0 & -\sin(\chi) & \cos(\chi) \end{pmatrix}. \quad (2.29)$$

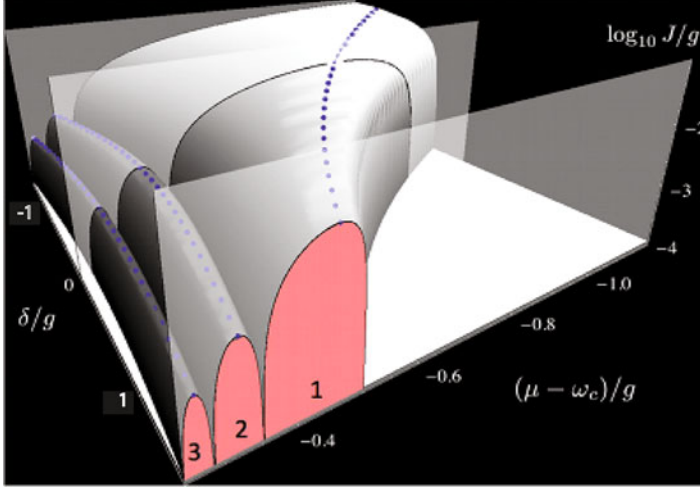


Fig. 2.3 Quantum phase diagram for the JCHM as obtained from slave-boson theory, i.e., Eq. (2.26). Shown are the lowest three Mott lobes with polariton numbers $N = 1, 2, 3$. Dotted lines represent the critical hopping strength's J_c/g for which the chemical potential μ and detuning δ are chosen such as to fulfill particle-hole symmetry. Finite detuning $|\delta| > 0$ decreases the critical hopping strength J_c/g for $N > 1$, but the lowest Mott lobe ($N = 1$) steadily increases when tuning through the resonance ($\delta = 0$). Figure taken with permission from [18] (with minor modifications)

The operator G^\dagger creates a new vacuum state, i.e., the mean-field ground state $|\psi\rangle = \prod_i G_i^\dagger |0\rangle$, and $E_{1i}^\dagger, E_{2i}^\dagger$ are orthogonal operators creating excitations above the ground-state. We express the Hamiltonian in terms of these new operators and eliminate G_i by using the constraint (2.21) in the restricted Hilbert space

$$G_i \approx \sqrt{1 - E_{1i}^\dagger E_{1i} - E_{2i}^\dagger E_{2i}} \quad (2.30)$$

Expanding the square root everywhere in the Hamiltonian to quadratic order in $E_{(1,2)i}^{(\dagger)}$ yields, after a Fourier transformation, an effective quadratic Hamiltonian

$$H_{\text{eff}} = \epsilon_{\text{var}} + \sum_{\mathbf{k}} \mathbf{E}_{\mathbf{k}}^\dagger h_{\text{eff},\mathbf{k}} \mathbf{E}_{\mathbf{k}} \quad (2.31)$$

where $\mathbf{E} = (E_{1\mathbf{k}}, E_{2\mathbf{k}}, E_{1-\mathbf{k}}^\dagger, E_{2-\mathbf{k}}^\dagger)^T$ and $h_{\text{eff},\mathbf{k}}$ is a 4×4 matrix

$$h_{\text{eff},\mathbf{k}} = \begin{pmatrix} g & f \\ f & g \end{pmatrix}, \quad (2.32)$$

with f, g denoting 2×2 matrices defined in the appendix. The sum over \mathbf{k} runs over the first Brillouin zone. The effective Hamiltonian can be diagonalized by a bosonic Bogoliubov transformation yielding

$$H_{\text{eff}} = \epsilon_{\text{var}} + \epsilon_{\text{fluct}} + \sum_{\alpha=\pm} \sum_{\mathbf{k}} \epsilon_{\alpha}(\mathbf{k}) d_{\alpha\mathbf{k}}^{\dagger} d_{\alpha\mathbf{k}} \quad (2.33)$$

with a fluctuation-generated correction of the ground-state energy

$$\epsilon_{\text{fluct}} = \mathcal{E}(\theta, \chi) + \sum_{\alpha=\pm} \sum_{\mathbf{k}} \epsilon_{\alpha}(\mathbf{k})/2 \quad (2.34)$$

and $d_{\alpha\mathbf{k}}^{\dagger}$ creating excitations with energy

$$\epsilon_{\pm}(\mathbf{k}) = \sqrt{A(\mathbf{k}) \pm \sqrt{A(\mathbf{k})^2 - B(\mathbf{k})}} \quad (2.35)$$

with rather lengthy expressions for $\mathcal{E}(\theta, \chi)$, $A(\mathbf{k})$, and $B(\mathbf{k})$ given in the appendix of Ref. [26]. In the Mott phase, these spectra agree with the expressions for particle/hole like modes in Eq. (2.16). In the superfluid phase, we obtain a gapless, linear Goldstone mode $\epsilon_{-}(\mathbf{k}) = c_s |\mathbf{k}| + \mathcal{O}(\mathbf{k}^2)$ with sound velocity c_s . A second mode, the so-called amplitude or Higgs mode, generally remains gapped with $\epsilon_{+}(\mathbf{k}) = \Delta_a + \mathcal{O}(\mathbf{k}^2)$ (except for the tip of the lobe). For a more detailed discussion of the excitation spectra we refer to the caption in Fig. 2.4.

2.5 Critical Exponents

In the previous two sections we have calculated the dispersion relations for the elementary excitations of the JCHM in the Mott and superfluid phases. The long wavelength behavior of the dispersion at $\mathbf{k} \rightarrow 0$ right at the phase boundary determines the dynamical critical exponent z defined by $\omega \sim \xi^{-z} \sim k^z$ with the diverging correlation length $\xi \sim |J - J_c|^{-\nu}$ and its associated critical exponent ν . If the phase boundary is approached away from the tip of the lobe, either the particle (upper phase boundary) or the hole (lower phase boundary) gap vanishes linearly $\Delta \sim |J - J_c|$ and the dispersion remains quadratic $\omega \sim k^2$. The situation changes at the tip of the lobe, where particle and hole gaps vanish simultaneously with a square-root behavior $\Delta \sim |J - J_c|^{1/2}$, while their dispersions become linear $\omega \sim k$ (see Fig. 2.4). This indicates a special transition at the tip of the lobe, reminiscent of an emergent particle-hole symmetry.

Consequently, according to the analytical results of the previous sections the dynamical critical exponent has the generic value $z = 2$ everywhere in the phase diagram except for the special critical point at the tip of the lobe where it changes to $z = 1$. At $\mathbf{k} = \mathbf{0}$ the gap vanishes as $\Delta \sim |J - J_c|^{z\nu}$ when the tunneling strength approaches its critical value J_c . This leads to a mean-field exponent $\nu = 1/2$ everywhere in the phase diagram. Thus on a mean-field level, the JCHM has the same critical exponents as the BHM [69] with a change of its universality class along the

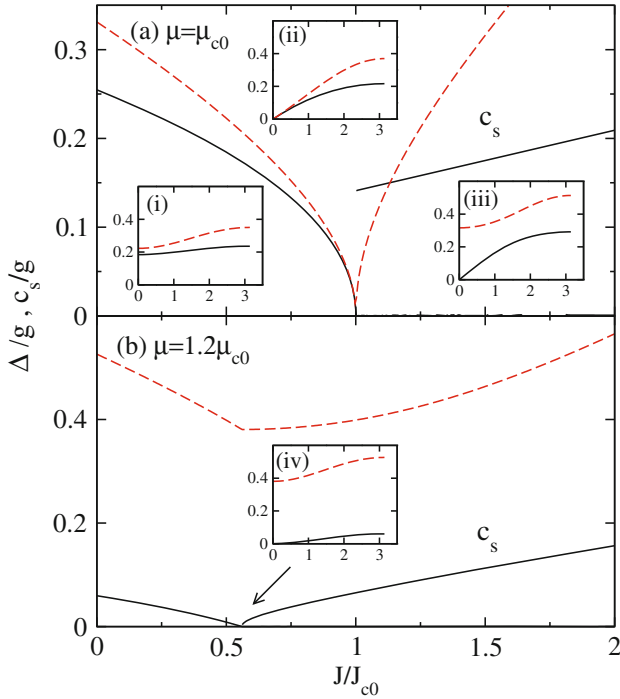


Fig. 2.4 Elementary excitations of the JCHM as a function of the effective hopping strength J/J_{c0} at zero detuning $\delta/g = 0$ and for **a** $\mu = \mu_{c0}$ where μ_{c0} denotes the critical chemical potential at the tip of the lobe with critical hopping strength $J_c = J_{c0}$ (*top figure*) and **b** away from the tip at $\mu = 1.2\mu_{c0}$ with $J_c = 0.566J_{c0}$ (*bottom figure*). Shown are the gaps of particle (*dashed*) and hole (*solid*) modes in the Mott phase ($J < J_c$) and as well as the gaps of the Amplitude mode (*dashed*) and the sound velocity of the Goldstone mode (*solid*). The insets show the corresponding excitation spectra at (i) $J = 0.5J_{c0}$ (in the Mott phase) (ii) $J = J_{c0}$ (at the tip of the lobe) (iii) $J = 1.5J_{c0}$ (in the superfluid phase) (iv) $J = 0.566J_{c0}$ (at the phase boundary away from the tip of the lobe). At the phase boundary, the particle and hole mode of the Mott phase are identical with the Goldstone and Amplitude modes of the superfluid phase. At the tip of the lobe (ii), where the polariton density can remain constant during the superfluid-insulator transition, the Amplitude mode becomes gapless and linear (its mass vanishes). The sound velocity of the Goldstone mode remains non-zero, confirming a special point in the phase diagram with dynamical critical exponent $z = 1$. Away from the tip (iv), the Amplitude mode remains gapped and the Goldstone mode becomes quadratic with a vanishing sound velocity corresponding to a generic dynamical critical exponent $z = 2$. Figure taken with permission from [18] (with minor modifications)

phase boundary. This result has also been predicted using scaling arguments based on an effective action approach [13].

However, early Quantum Monte Carlo (QMC) calculations of the superfluid density [11] suggested that the universality class at the tip of the Mott lobe of the JCHM is different from the BHM. This controversy between analytical and numerical findings has been resolved in Ref. [20] in favour of the early analytical arguments in Refs. [12, 13]. In Ref. [20] extensive QMC simulations of the superfluid density

and the compressibility were carried out on the two-dimensional square lattice by using much larger system sizes as compared to previous studies. Below we briefly summarise these results.

The finite-size scaling form of the superfluid density ρ_s is known from Ref. [69] and reads

$$\rho_s = L^{2-D-z} \tilde{\rho}_s[(J - J_c)L^{1/\nu}, \beta/L^z]. \quad (2.36)$$

Fixing the ratio $\alpha = \beta/L^z$, the quantity

$$X_{z\nu}(L) = L^{D-2+z} \rho_s[(J - J_c)L^{1/\nu}, \alpha] = \tilde{\rho}_s[(J - J_c)L^{1/\nu}, \alpha] \quad (2.37)$$

depends only on the distance from the critical point, i.e., $(J - J_c)L^{1/\nu}$. Thus plotting $X_{z\nu}(L)$ as a function of J for different system sizes L allows us to determine the critical value J_c , where curves for different L intersect. In Ref. [20] this quantity has been calculated via QMC simulations using world lines in the stochastic series expansion (SSE) representation (see Ref. [14] and references therein).

Figure 2.5a shows the rescaled superfluid density $\rho_s L$ as a function of the hopping strength J/g assuming $z = 1$ for system sizes ranging from 20×20 to 40×40 . The intersect of the curves leads to the estimate of the critical hopping strength $J_c/g = 0.05241(1)$. Figure 2.5b shows $X_{z\nu}(L)$ as a function of $(J - J_c)L^{1/\nu}$. One observes a clear scaling collapse as expected from Eq. (2.37). Note, that here a correlation length exponent $\nu = 0.6715$ (as found numerically for the BHM [77]) has been assumed. We can thus conclude that universal scaling at the tip of the lobe is observed for a dynamical critical exponent $z = 1$ confirming unambiguously the prediction of the analytical calculations in Refs. [12, 13].

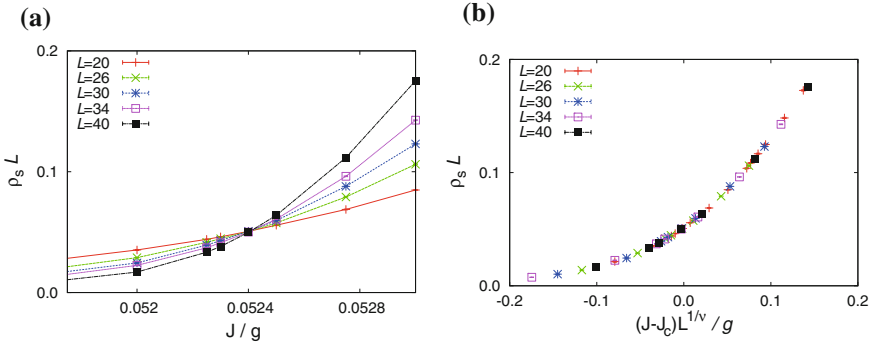


Fig. 2.5 (Color online) Scaling of the superfluid density ρ_s across the fixed-density transition at the tip of the lobe with $\mu/g = 0.185$ [11] using $L \times L$ square lattices and $\beta g = 2L$. The intersect of $L\rho_s$ for different lattice sizes L in a single point in panel **a** is evidence for a dynamical critical exponent $z = 1$, and defines the critical point at $J_c/g = 0.05242(1)$. **b** Scaling collapse using $J_c/g = 0.05242$ and the exact critical exponent $\nu = 0.6715$ [77]. Figure taken with permission from Ref. [20]

2.6 Relation to the Dicke Model

In this section we discuss a remarkable relation between the superfluid-Mott insulator transition of polaritons in coupled qubit-cavity arrays and the superradiance phase transition of the Tavis-Cummings or Dicke model [78–82]. In particular, we argue that a weak-coupling mean-field theory for the Dicke model predicts the existence of a single Mott lobe, where the universality class of the phase transition changes at the tip of the lobe just as for the JCHM [26].

The Dicke model describes the interaction of a single photonic mode with a number of N_s qubits and can be written as

$$H = \tilde{\omega}_c a_0^\dagger a_0 + \tilde{\omega}_x \sum_i \sigma_i^+ \sigma_i^- + \frac{g}{\sqrt{N_s}} \sum_i (\sigma_i^+ a_0 + \text{h.c.}) , \quad (2.38)$$

where we have also introduced a Dicke model chemical potential μ_D for polaritons according to the recipe in Eq. (2.3) leading to the definition $\tilde{\omega}_c = \omega_c - \mu_D$ and $\tilde{\omega}_x = \omega_x - \mu_D$. A weak-coupling mean-field theory for the Dicke model (at zero temperature and in a frame rotating at the cavity frequency ω_c) predicts a phase transition from a normal phase with $\psi = \langle a_0 \rangle = 0$ to a superradiant state with $\psi \neq 0$ at the critical coupling strength [79, 81]

$$g^2 = -\mu_D |\delta_D - \mu_D| . \quad (2.39)$$

However, for $\mu_D > \delta_D$ and negative detuning $\delta_D < 0$ we observe the appearance of a second normal phase corresponding to a Mott lobe with all two-level systems inverted, i.e., with one excitation per cavity ($n = 1$) [26]. The corresponding zero temperature phase diagram is shown in Fig. 2.6. The phase boundary of this lobe can be obtained from Eq. (2.39) as

$$\mu_D = \frac{1}{2} \left(\delta_D \pm \sqrt{\delta_D^2 - 4g^2} \right) . \quad (2.40)$$

with the tip of the lobe at $\delta_D = -2g$ and $\mu_D = -g$.

We now argue that this interesting result can be understood as a special limit of the JCHM: We first Fourier transform the photon operators in Eq. (2.1) to momentum space

$$a_i = \frac{1}{\sqrt{N_s}} \sum_{\mathbf{k}} a_{\mathbf{k}} e^{i\mathbf{k} \cdot \mathbf{r}_i} \quad (2.41)$$

such that the JCHM can be written as

$$H = \sum_{\mathbf{k}} \tilde{\omega}_{\mathbf{k}} a_{\mathbf{k}}^\dagger a_{\mathbf{k}} + \sum_i \tilde{\omega}_x \sigma_i^+ \sigma_i^- + \sum_{i\mathbf{k}} \frac{g_{i\mathbf{k}}}{\sqrt{N_s}} (\sigma_i^+ a_{\mathbf{k}} + \text{h.c.}) \quad (2.42)$$

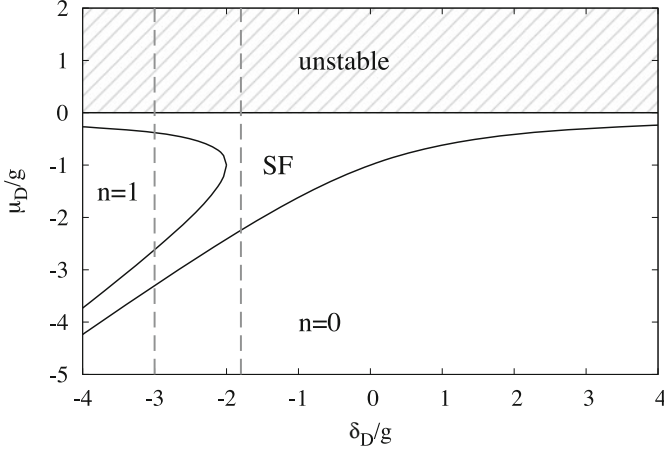


Fig. 2.6 Quantum phase diagram of the Dicke model and the JCHM at infinite bandwidth and infinite negative detuning for fixed μ_D , δ_D (see text) showing the transition from the vacuum ($n = 0$) to a superfluid state as well as the existence of a single Mott lobe with $n = 1$. Figure taken with permission from Ref. [26]

where $\tilde{\omega}_{\mathbf{k}} = \tilde{\omega}_c - 2J \sum_{\alpha=1}^D \cos(k_{\alpha})$ with $\tilde{\omega}_c = \omega_c - \mu$, $\tilde{\omega}_x = \omega_x - \mu$ and $g_{i\mathbf{k}} = g e^{i\mathbf{k} \cdot \mathbf{r}_i}$ (N_s denotes the number of lattice sites). This Hamiltonian represents a many-mode Dicke model, as studied in Refs. [83, 84]. The case studied in those works, however, considered a quadratic photon spectrum, equivalent to expanding the lattice dispersion for small \mathbf{k} vectors yielding

$$\tilde{\omega}_{\mathbf{k}} = \tilde{\omega}_c - 2DJ + J\mathbf{k}^2 \equiv J\mathbf{k}^2 - \mu_D, \quad (2.43)$$

where we have defined a Dicke-model chemical potential $\mu_D = \mu + 2DJ - \omega_c$ (such that $\mu_D < 0$ is required for thermodynamic stability). Following Ref. [26], it is also useful to define a Dicke-model detuning $\delta_D = \delta + 2DJ$, which measures the detuning between the qubit (2LS) energy and the bottom of the photon band so that $\tilde{\omega}_x = \delta_D - \mu_D$. With this quadratic expansion the generalised Dicke model in (2.42) describes N_s localised two-level systems coherently coupled to a continuum of photonic modes with an effective photonic mass $1/2J$. Note, that if one neglects all finite momentum modes, Eq. (2.42) reduces to the single-mode Dicke model in Eq. (2.38) with $a_0 = a_{\mathbf{k}=0}$.

Thus, if one considers the limit of infinite bandwidth $J \rightarrow \infty$ and infinite negative detuning $\delta \rightarrow -\infty$, the ground state of the JCHM at fixed chemical potential will mostly be composed of qubit excitations such that higher k modes can be neglected. In that case we expect that the long wavelength physics of the JCHM is similar to the Dicke model. Indeed, in Ref. [26] we have shown that if one takes the limit of infinite bandwidth and negative detuning such that μ_D and δ_D remain fixed, the phase diagram in Fig. 2.3 maps exactly to the one in Fig. 2.6. This is a remarkable connection

since both phase diagrams have been derived using very different methods, i.e., a weak-coupling mean-field theory on one hand and a strong-coupling slave-boson theory on the other. Moreover, also the excitation spectra as calculated from both theories match exactly at the phase boundary of the Mott lobe [26]. In Fig. 2.3 one can see the reason for this success: the size of the lowest Mott lobe increases for large J and large negative detuning δ , while the size of all other lobes decreases. Thus, only one lobe survives in Fig. 2.6. All other modes are pushed towards $\mu_D = 0$ and vanish. This is in strong contrast to the Bose-Hubbard model, where a weak-coupling Bogoliubov-like theory describing weakly interacting atomic BEC's, fails to predict the existence of Mott lobes and gapped Higgs-like modes [85].

Acknowledgements We thank Martin Hohenadler, Markus Aichhorn, Jonathan Keeling and Lode Pollet for valuable discussions. This work was supported by a Ambizione award (S.S.) of the Swiss National Science Foundation.

References

1. A.D. Greentree, C. Tahan, J.H. Cole, L. Hollenberg, *Nat. Phys.* **2**, 856 (2006)
2. D. Angelakis, M. Santos, S. Bose, *Phys. Rev. A* **76**, 031805 (2007)
3. J. Cho, D.G. Angelakis, S. Bose, *Phys. Rev. A* **78**, 062338 (2008)
4. G. Zhu, S. Schmidt, J. Koch, *New J. Phys.* **15**, 115002 (2013)
5. M. Hartmann, F. Brandão, M. Plenio, *Phys. Rev. Lett.* **99**, 160501 (2007)
6. M. Hartmann, F. Brandão, M. Plenio, *Nat. Phys.* **2**, 849–855 (2006)
7. D. Rossini, R. Fazio, *Phys. Rev. Lett.* **99**, 186401 (2007)
8. D. Rossini, R. Fazio, G. Santoro, *Europhys. Lett.* **83**, 47011 (2008)
9. M. Aichhorn, M. Hohenadler, C. Tahan, P. Littlewood, *Phys. Rev. Lett.* **100**, 216401 (2008)
10. M.J. Hartmann, F.G.S.L. Brandao, M.B. Plenio, *New J. Phys.* **10**, 033011 (2008)
11. J. Zhao, A.W. Sandvik, K. Ueda (2008). [arXiv:0806.3603](https://arxiv.org/abs/0806.3603)
12. S. Schmidt, G. Blatter, *Phys. Rev. Lett.* **103**, 086403 (2009)
13. J. Koch, K.L. Hur, *Phys. Rev. A* **80**, 023811 (2009)
14. P. Pippian, H. Evertz, M. Hohenadler, *Phys. Rev. A* **80**, 033612 (2009)
15. P.A. Ivanov, S.S. Ivanov, N.V. Vitanov, A. Mering, M. Fleischhauer, K. Singer, *Phys. Rev. A* **80**, 060301 (2009)
16. M. Knap, E. Arrigoni, W. von der Linden, *Phys. Rev. B* **81**, 104303 (2010)
17. M. Knap, E. Arrigoni, W. von der Linden, *Phys. Rev. B* **82**, 045126 (2010)
18. S. Schmidt, G. Blatter, *Phys. Rev. Lett.* **104**, 216402 (2010)
19. A. Tomadin, V. Giovannetti, R. Fazio, D. Gerace, I. Carusotto, H. Türeci, A. Imamoglu, *Phys. Rev. A* **81**, 061801 (2010)
20. M. Hohenadler, M. Aichhorn, S. Schmidt, L. Pollet, *Phys. Rev. A* **84**, 041608(R) (2011)
21. K. Liu, L. Tan, C.H. Lv, W.M. Liu, *Phys. Rev. A* **83**, 063840 (2011)
22. M. Hohenadler, M. Aichhorn, L. Pollet, S. Schmidt, *Phys. Rev. A* **85**, 013810 (2012)
23. C. Nietner, A. Pelster, *Phys. Rev. A* **85**, 043831 (2012)
24. M. Schiró, M. Bordyuh, B. Öztóp, H.E. Türeci, *Phys. Rev. Lett.* **109**, 053601 (2012)
25. F. Nissen, S. Schmidt, M. Biondi, G. Blatter, H.E. Türeci, J. Keeling, *Phys. Rev. Lett.* **108**, 233603 (2012)
26. S. Schmidt, G. Blatter, J. Keeling, *J. Phys. B: At. Mol. Opt. Phys.* **46**, 224020 (2013)
27. T. Grujic, S.R. Clark, D. Jaksch, D.G. Angelakis, *Phys. Rev. A* **87**, 053846 (2013)
28. T. Yuge, K. Kamide, M. Yamaguchi, T. Ogawa (2014). [arXiv:1401.6229](https://arxiv.org/abs/1401.6229)
29. D. Sarchi, I. Carusotto, M. Wouters, V. Savona, *Phys. Rev. B* **77**, 125324 (2008)

30. D. Gerace, H.E. Türeci, A. Imamoglu, V. Giovannetti, R. Fazio, *Nat. Phys.* **5**, 281–284 (2009)
31. S. Schmidt, D. Gerace, A. Houck, G. Blatter, H.E. Türeci, *Phys. Rev. B* **82**, 100507 (2010)
32. N. Schetakakis, T. Grujic, S. Clark, D. Jaksch, D. Angelakis, *J. Phys. B: At. Mol. Opt. Phys.* **46**, 224025 (2013)
33. J. Raftery, D. Sadri, S. Schmidt, H.E. Türeci, A.A. Houck (2013). [arXiv:1312.2963](https://arxiv.org/abs/1312.2963)
34. M. Hartmann, *Phys. Rev. Lett.* **104**, 113601 (2010)
35. T. Grujic, S.R. Clark, D.G. Angelakis, D. Jaksch, *New J. Phys.* **14**, 103025 (2012)
36. A.L. Boité, G. Orso, C. Ciuti, *Phys. Rev. Lett.* **110**, 233601 (2013)
37. J. Jin, D. Rossini, R. Fazio, M. Leib, M.J. Hartmann, *Phys. Rev. Lett.* **110**, 163605 (2013)
38. I. Carusotto, D. Gerace, H.E. Türeci, S. De Liberato, C. Ciuti, A. Imamoglu, *Phys. Rev. Lett.* **103**, 033601 (2009)
39. M. Kiffner, M. Hartmann, *Phys. Rev. A* **81**, 021806 (2010)
40. A.G. D'Souza, B.C. Sanders, D.L. Feder, *Phys. Rev. A* **88**, 063801 (2013)
41. J. Koch, A. Houck, K. Le Hur, S. Girvin, *Phys. Rev. A* **82**, 043811 (2010)
42. A. Nunnenkamp, J. Koch, S.M. Girvin, *New J. Phys.* **13**, 095008 (2011)
43. M. Hafezi, E.A. Demler, M.D. Lukin, J.M. Taylor, *Nat. Phys.* **7**, 907–912 (2011)
44. A. Kamal, J. Clarke, M.H. Devoret, *Nat. Phys.* **7**, 311–315 (2011)
45. R.O. Umucalilar, I. Carusotto, *Phys. Rev. Lett.* **108**, 206809 (2012)
46. M. Hafezi, S. Mittal, J. Fan, A. Migdall, J.M. Taylor, *Nat. Photon* **7**, 1001–1005 (2013)
47. C.E. Bardyn, S.D. Huber, O. Zilberberg (2013). [arXiv:1312.6894](https://arxiv.org/abs/1312.6894)
48. A. Petrescu, A.A. Houck, K. Le Hur, *Phys. Rev. A* **86**, 053804 (2012)
49. C.E. Bardyn, A. Imamoglu, *Phys. Rev. Lett.* **109**, 253606 (2012)
50. M.J. Hwang, M.S. Choi, *Phys. Rev. B* **87**, 125404 (2013)
51. B. Kumar, S. Jalal, *Phys. Rev. A* **88**, 011802 (2013)
52. A.A. Zvyagin, *Phys. Rev. Lett.* **110**, 217207 (2013)
53. J. Cho, D. Angelakis, S. Bose, *Phys. Rev. Lett.* **101**, 246809 (2008)
54. A. Hayward, A.M. Martin, A.D. Greentree, *Phys. Rev. Lett.* **108**, 223602 (2012)
55. M. Hafezi, M.D. Lukin, J.M. Taylor, *New J. Phys.* **15**, 063001 (2013)
56. R.O. Umucalilar, M. Wouters, I. Carusotto, *Phys. Rev. A* **89**, 023803 (2014)
57. M. Hartmann, F. Brandão, M. Plenio, *Laser Photonics Rev.* **2**, 527–556 (2008)
58. A. Tomadin, R. Fazio, *J. Opt. Soc. Am. B* **27**, 130–136 (2010)
59. A.A. Houck, H.E. Türeci, J. Koch, *Nat. Phys.* **8**, 292–299 (2012)
60. I. Carusotto, C. Ciuti, *Rev. Mod. Phys.* **85**, 299 (2013)
61. S. Schmidt, J. Koch, *Annalen der Physik* **525**, 395–412 (2013)
62. D.L. Underwood, W.E. Shanks, J. Koch, A.A. Houck, *Phys. Rev. A* **86**, 023837 (2012)
63. J. Klaers, J. Schmitt, F. Vewinger, M. Weitz, *Nature* **468**, 545–548 (2010)
64. P. Kirtan, J. Keeling, *Phys. Rev. Lett.* **111**(Sep), 100404 (2013)
65. J. Schmitt, T. Damm, D. Dung, F. Vewinger, J. Klaers, M. Weitz, *Phys. Rev. Lett.* **112**(Jan), 030401 (2014)
66. J. Klaers, J. Schmitt, T. Damm, D. Dung, F. Vewinger, M. Weitz, *Proc. SPIE* **8600**, 8600L (2013)
67. H. Deng, H. Haug, Y. Yamamoto, *Rev. Mod. Phys.* **82**, 1489 (2010)
68. O. Astafiev, A.M. Zagoskin, A.A. Abdumalikov, Y.A. Pashkin, T. Yamamoto, K. Inomata, Y. Nakamura, J.S. Tsai, *Science* **327**, 840 (2010)
69. M.P.A. Fisher, P.B. Weichman, J. Watson, D.S. Fisher, G. Grinstein, *Phys. Rev. B* **40**, 546 (1989)
70. H. Kleinert, *Path Integrals in Quantum Mechanics, Statistics, Polymer Physics, and Financial Markets* (World Scientific, Singapore, 2006)
71. H. Kleinert, S. Schmidt, A. Pelster, *Annalen der Physik* **14**, 214 (2005)
72. F.E.A. dos Santos, A. Pelster, *Phys. Rev. A* **79**, 013614 (2009)
73. N. Teichmann, D. Hinrichs, M. Holthaus, A. Eckardt, *Phys. Rev. B* **79**, 100503 (2009)
74. W. Metzner, *Phys. Rev. B* **43**, 8549 (1991)
75. M. Ohliger, A. Pelster (2008). [arXiv:0810.4399](https://arxiv.org/abs/0810.4399)
76. S.D. Huber, E. Altman, H.P. Büchler, G. Blatter, *Phys. Rev. B* **75**, 085106 (2007)

- 77. B. Capogrosso-Sansone, S.G. Söyler, N. Prokof'ev, B. Svistunov, Phys. Rev. B **77**, 015602 (2008)
- 78. R. Dicke, Phys. Rev. **93**, 99–110 (1954)
- 79. K. Hepp, E.H. Lieb, Ann. Phys. **76**, 360–404 (1973)
- 80. Y.K. Wang, F.T. Hioe, Phys. Rev. A **7**, 831 (1973)
- 81. K. Hepp, E. Lieb, Phys. Rev. A **8**, 2517–2525 (1973)
- 82. M. Tavis, F.W. Cummings, Phys. Rev. **170**, 379 (1968)
- 83. J. Keeling, P.R. Eastham, M.H. Szymanska, P.B. Littlewood, Phys. Rev. Lett. **93**, 226403 (2004)
- 84. J. Keeling, P.R. Eastham, M.H. Szymanska, P.B. Littlewood, Phys. Rev. B **72**, 115320 (2005)
- 85. D. van Oosten, P. van der Straten, H.T.C. Stoof, Phys. Rev. A **63**, 053601 (2001)

Quantum Simulations with Photons and Polaritons
Merging Quantum Optics with Condensed Matter
Physics

Angelakis, D.G. (Ed.)

2017, XIII, 214 p. 86 illus., 77 illus. in color., Hardcover

ISBN: 978-3-319-52023-0